Quantitative multi-layer electromagnetic induction inversion and full-waveform inversion of crosshole ground penetrating radar data

Jan van der Kruk[1,2] , Nils Gueting[1], Anja Klotzsche[1,2], Guowei He[1,2], Sebastian Rudolph[1], Christian von Hebel[1,2], Xi Yang[1], Lutz Weihermüller[1], Achim Mester[3], and Harry Vereecken[1,2]

[1]*Agrosphere (IBG-3), Forschungszentrum Jülich GmbH, Jülich, Germany*

[2] *Centre for High-Performance Scientific Computing in Terrestrial Systems (TerrSys)*

[3] *Electronic Systems (ZEA-2), Forschungszentrum Jülich GmbH, Jülich, Germany*

Abstract

Due to the recent system developments for the electromagnetic characterization of the subsurface, fast and easy acquisition is made feasible due to the fast measurement speed, easy coupling with GPS systems, and the availability of multi-channel electromagnetic induction (EMI) and ground penetrating radar (GPR) systems. Moreover, the increasing computer power enables the use of accurate forward modeling programs in advanced inversion algorithms where no approximations are used and the full information content of the measured data can be exploited. Here, recent developments of large-scale quantitative EMI inversion and full-waveform GPR inversion are discussed that yield higher resolution of quantitative medium properties compared to conventional approaches. In both cases a detailed forward model is used in the inversion procedure that is based on Maxwell's equations. The multi-channel EMI data that have different sensing depths for the different source-receiver offset are calibrated using a short electrical resistivity tomography (ERT) calibration line which makes it possible to invert for electrical conductivity changes with depth over large areas. The crosshole GPR full-waveform inversion yield significant higher resolution of the permittivity and conductivity images compared to ray-based inversion results.

Keywords: Ground Penetrating Radar, Electromagnetic Induction, Full-waveform inversion.

Introduction

The electromagnetic tools, EMI and GPR, can be used for a wide range of applications to non-invasively image the subsurface. Due to the fast data acquisition, where the measured data can be directly linked with high resolution GPS systems, it is becoming more and more feasible to map GPR and EMI over large areas. The use of multi-channel EMI and GPR makes it possible to acquire simultaneously EMI and GPR data for different source-receiver offsets that enable an improved subsurface characterization. Ray-based or approximate techniques are often used where only part of the data is exploited. Improved subsurface characterization can be obtained by including advanced modeling tools that are able to calculate the electromagnetic wave propagation with high accuracy using Maxwell's equations. In the following, we will describe recent advancements in the high-resolution imaging of EMI and GPR data.

Quantitative multi-configuration multi-layer EMI inversion

EMI measurements are often performed with single source-receiver systems to qualitatively map the spatial apparent electrical conductivity (ECa) patterns and to relate them with the soil properties (e.g. Abdu et al., 2008). Recently, new generation multi-configuration EMI systems have become commercially available which consist of multiple coils with different separations and different orientations (Santos et al., 2010; Saey et al., 2012, Rudolph et al., 2015, Stadler et al., 2015). Since the measured ECa is a weighted average value over the coil configuration specific penetration depth, this enables a simultaneous sensing over different depth ranges. In principle, these multi-configuration data can be used to obtain electrical conductivity changes with depth. However, for a reliable inversion, the measured ECa values needs to be quantitative, which is often not the case because EMI data can significantly be affected by external influences that alter EMI measurements, such as the presence of the operator or cables near the coils, and the field set-up used to move the EMI system (Robinson et al., 2004; Nüsch et al., 2010). One option to obtain reliable ECa measurements with EMI it to calibrate the data using inverted ERT data measured together with EMI along the same profile. Using this data as input in a Maxwell-based full-solution forward model, the predicted apparent electrical conductivities are used to calibrate the measured data using linear regression parameters (Lavoué et al., 2010).

Instead of applying an inversion algorithm that is based on the low induction number approximation, we invert large-scale multi-configuration EMI data using a Maxwell-based full-solution EM forward model to resolve the 3D multi-layer electrical conductivity structures. Based on the two-layer inversion as discussed by Mester et al. (2011), an improved three-layer inversion scheme was developed (von Hebel et al., 2014) that explores the information content of M=6 different EMI data configurations and minimizes the normalized misfit between the measured magnetic field H_m^{mea}, and the modeled magnetic field $H_m^{mod}(\boldsymbol{p})$;

$$\Delta H(\boldsymbol{p}) = \frac{1}{M}\sum_{m=1}^{M} \frac{|H_m^{mea} - H_m^{mod}(\boldsymbol{p})|}{|H_m^{mea}(\boldsymbol{p})|} \quad (1)$$

Here, the modeled magnetic field is calculated using a full-solution horizontally layered EM forward model (von Hebel et al., 2014), and $\mathbf{p}$ contains the three-layer parameters σ_1, σ_2, σ_3, h_1, and h_2 that are being optimized using an efficient parallelized global minimization algorithm, the shuffled complex evolution (SCE) algorithm (see von Hebel et al. (2014) for more details about the used inversion algorithm).

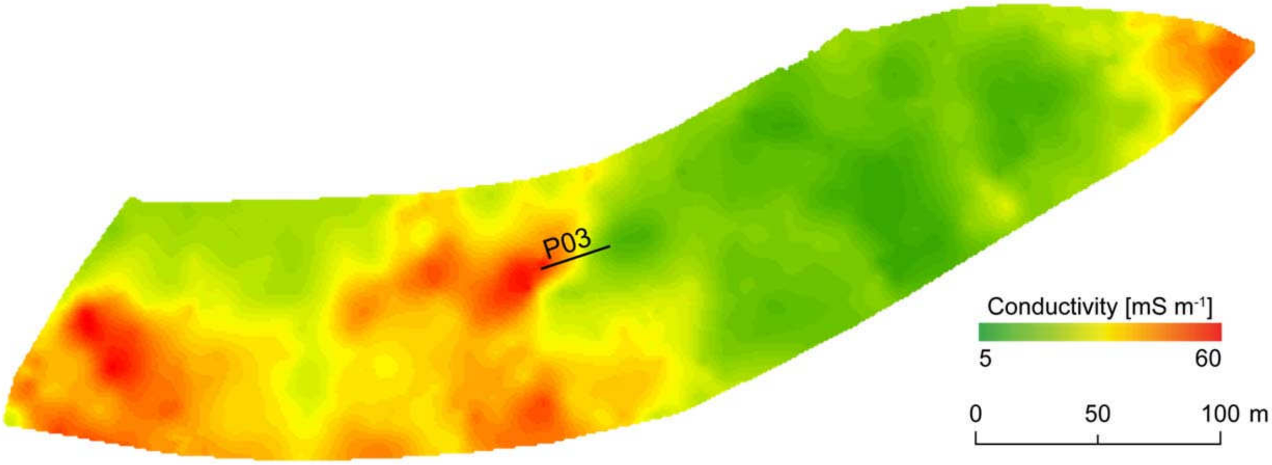

Figure 1. Interpolated large-scale ECa measurements using the VCP configuration and a source-receiver distance of 1.18m. Along the P03 transect, where large ranges of ECa values were present, an ERT profile of 30 m was measured to enable the calibration of the EMI data. The ERT inversion results are shown in Figure 2.

At the Scheyern testsite (Germany), ECa measurements were performed using the CMD-MiniExplorer (GFinstruments, Brno, Czech Republic). The sensor consists of three receiver coils separated by 0.32, 0.71, and 1.18m from the transmitter coil resulting in a theoretical depth of exploration (DOE) of 0.25, 0.5, and 0.9 m in the vertical coplanar (VCP) and 0.5, 1.1, and 1.8 m for the horizontal coplanar (HCP) mode, respectively.

Figure 1 shows interpolated large-scale ECa values measured for a coil distance of 1.18m and VCP configuration which clearly indicates lateral changes in apparent electrical conductivity. Due to the influence of the operator and cables close to the EMI sensor, the measured apparent conductivity values can only be qualitatively interpreted. Inverting the multi-configuration EMI data result in unreliable inversion results (not shown). To calibrate the EMI data, reference line P03 was selected that contains lateral changes in conductivity as shown in Figure 1. Here, ERT measurements were performed over 30 m using electrode distances of 0.25 m. Figure 2 clearly shows the lateral and vertical changes in conductivity obtained by inverting the ERT data. The ERT data were used to calibrate the measured data (Lavoué et al. 2010) and to obtain quantitative EMI data. The calibrated data were inverted using a novel three-layer inversion that uses the shuffled complex evolution (SCE) optimization and a Maxwell-based electromagnetic forward model (von Hebel et al., 2014). The three-layer inversion results that are shown in Figure 3 approximate well the quantitative values for the different layers of the ERT structures. The dipping 2D structure between 20 and 25 m is less well reconstructed due to the horizontal layer assumption. Note that the EMI measurements were carried out in only a fraction of the time needed to perform the ERT measurements. Recently it was shown that the obtained calibration parameters can be applied to large scale data, where for each grid location the experimental EMI data are independently inverted and stitched together to form a quasi-3D image (von Hebel et al., 2014).

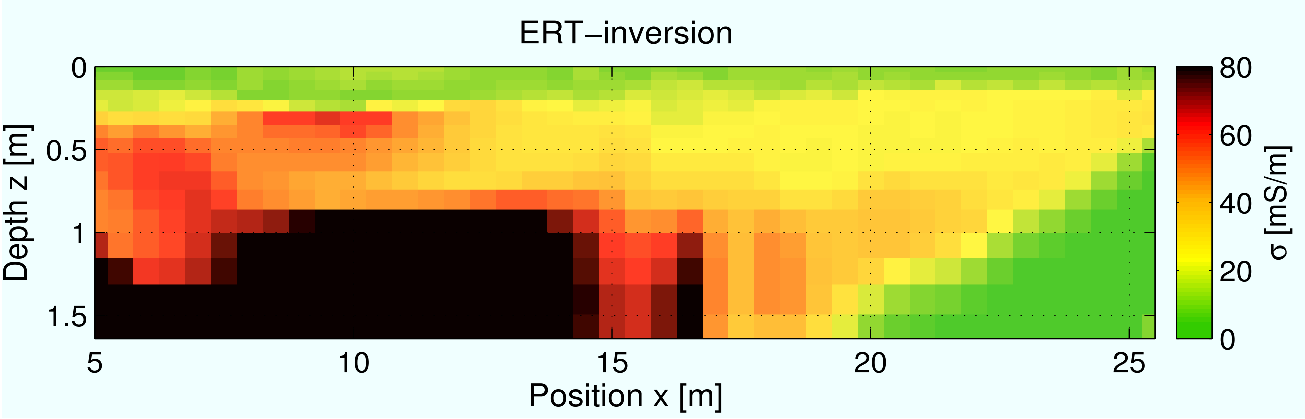

Figure 2. ERT-inversion results along the line P03 in Figure 1, where lateral and vertical changes in electrical conductivity are clearly visible.

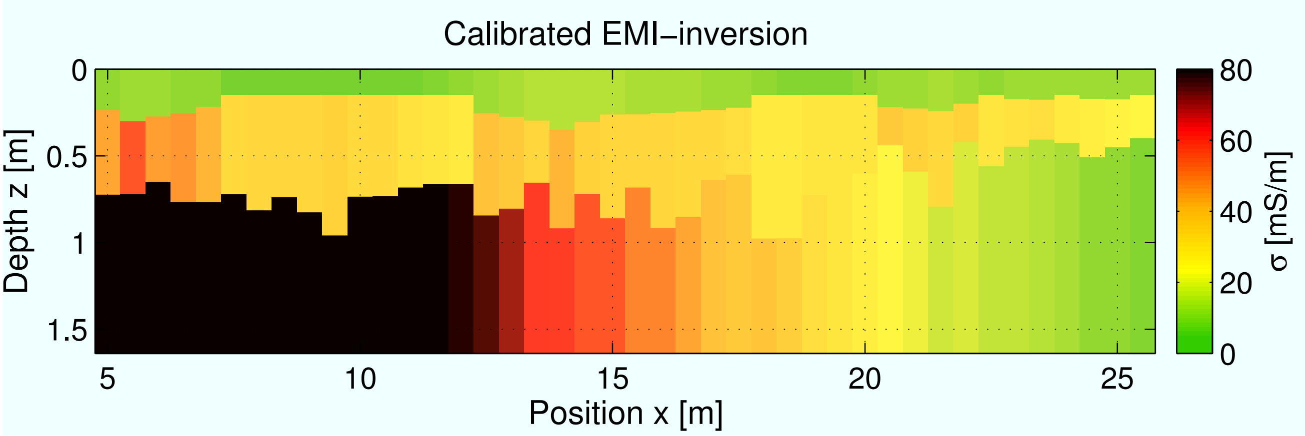

Figure 3. Inversion results of the calibrated multi-configuration EMI data that show similar quantitative conductivity values for the different layers as indicated by the ERT structures in Figure 2.

Full-waveform inversion of crosshole GPR data

Within the seismic community the full-waveform inversion (FWI) has found widespread applications (Virieux and Operto, 2009). In contrast, FWI methods for GPR are still fairly new. One of the first implementations of crosshole GPR full-waveform inversion (Ernst et al., 2007) is a conjugate gradient optimization algorithm in time domain. A vectorial approach was implemented that honors the vectorial electromagnetic wave propagation and simultaneously updates the permittivity and conductivity (Meles et al., 2010, 2011). Recently, a modified misfit and corresponding gradient equations have been introduced (Yang et al., 2013a) that do not depend anymore on the number of sources and receivers used. The modified misfit and adapted by Yang et al. (2013a) is defined as

$$\bar{S}(\varepsilon,\sigma) = \frac{1}{2}\sum_s \sum_r \sum_\tau \frac{[E^S_{syn}(\varepsilon,\sigma)-E^S_{obs}]^T_{r,\tau}\cdot[E^S_{syn}(\varepsilon,\sigma)-E^S_{obs}]_{r,\tau}}{N_S N_r}, \tag{2}$$

where $\mathrm{E}^{\mathrm{s}}_{\mathrm{syn}}(\varepsilon,\sigma)$ and $\mathrm{E}^{\mathrm{s}}_{\mathrm{obs}}$ are the synthetic and observed data, respectively, that contain the data for all sources, receivers and observation times according to the Meles et al., (2010) formalism. Here, T denotes the transpose conjugate and the synthetic data are calculated using a 2D finite-difference time-domain (FDTD) solution of Maxwell's equations. The gradients of the misfit function with respect to the permittivity and conductivity $\nabla\bar{S}_\varepsilon$, and $\nabla\bar{S}_\sigma$ are obtained by cross-correlating the incident wave field emitted from the source with the residual wave fields ΔE^S that are back-propagating using the back-propagation operator $\hat{G}^T$ from the receiver at all medium locations in the time domain for all sources and receiver combinations as follows (see also Meles et al., 2010 and Yang et al., 2013):

$$\begin{bmatrix}\nabla\bar{S}_\varepsilon(\varepsilon,\sigma)\\ \nabla\bar{S}_\sigma(\varepsilon,\sigma)\end{bmatrix} = \frac{1}{2N_S N_r}\sum_s \sum_r \sum_\tau \begin{matrix}(\partial_t E^S)^T\hat{G}^T[\Delta E^S]_{r,\tau}\\ (E^S)^T\hat{G}^T[\Delta E^S]_{r,\tau}\end{matrix} \tag{3}$$

Using these gradient directions, the update directions d_ε and d_σ are computed using the conjugate gradient method whereas the steplengths ζ_ε and ζ_σ are computed using a linear step length calculation and carefully chosen perturbation factors (see also Meles et al., 2010 and Yang et al., 2013). Finally, the model parameters are updated using

$$\begin{matrix}\varepsilon^{(k+1)}\\ \sigma^{(k+1)}\end{matrix} = \begin{matrix}\varepsilon^{(k)} - \zeta^{(k)}_\varepsilon d^{(k)}_\varepsilon\\ \sigma^{(k)} - \zeta^{(k)}_\sigma d^{(k)}_\sigma\end{matrix} \tag{4}$$

where k is the iteration number.

To apply the full-waveform method to experimental data and to invert the data using 2D forward model, a 3D to 2D conversion is required and an effective source wavelet must be estimated (Klotzsche et al., 2010). The starting relative permittivity and conductivity tomograms are usually obtained using standard ray-based inversion that is employing the first-arrival times and first-cycle amplitudes. Applying the full-waveform inversion on several crosshole GPR data sets acquired in gravel aquifers in Switzerland and the U.S.A. shows that sub-wavelength thickness low-velocity waveguiding layers can be correctly imaged (Klotzsche et al., 2012, 2013, 2014), whereas ray-based inversion techniques are not able to image these thin waveguide layers because they only exploit the first-arrival times and first-cycle amplitudes. Converting the permittivity results into porosity and comparing them with Neutron–Neutron logging data showed a good correspondence (Klotzsche et al., 2013, 2014).

Different versions of the full-waveform inversion were compared and applied to an experimental data set acquired at the Boise Hydrogeophysics Research Site (Yang et al., 2013). The obtained results show that most improvements results in a reduced final misfit between the measured and synthetic data and a reduced remaining gradient at the final iteration. Regions with relatively high remaining gradient amplitudes indicate less reliable inversion results. Frequency-domain full-waveform approaches have been recently implemented by Yang et al. (2013b) and Lavoue et al. (2014). Although here, selected frequencies can be used for the inversion to reduce the computational demands, selecting the appropriate frequencies is not straightforward.

Recently, many crosshole measurements were carried out at the Krauthausen testsite in Germany.

For a transect covering 25 m length and 10 m depth consisting of 5 crosshole planes, GPR data were inverted using the ray-based and full-waveform inversion as described by Klotzsche et al., (2010, 2013) and Oberrohrmann et al., (2013). Densely spaced cone penetration tests (CPT), located close to the GPR transect, were used to validate and interpret the obtained images obtained from GPR. A strong correlation was observed between CPT porosity logs and porosity estimates derived from GPR, whereas a less pronounced correlation was observed between electrical conductivity data derived from GPR and CPT (Gueting et al., 2015).

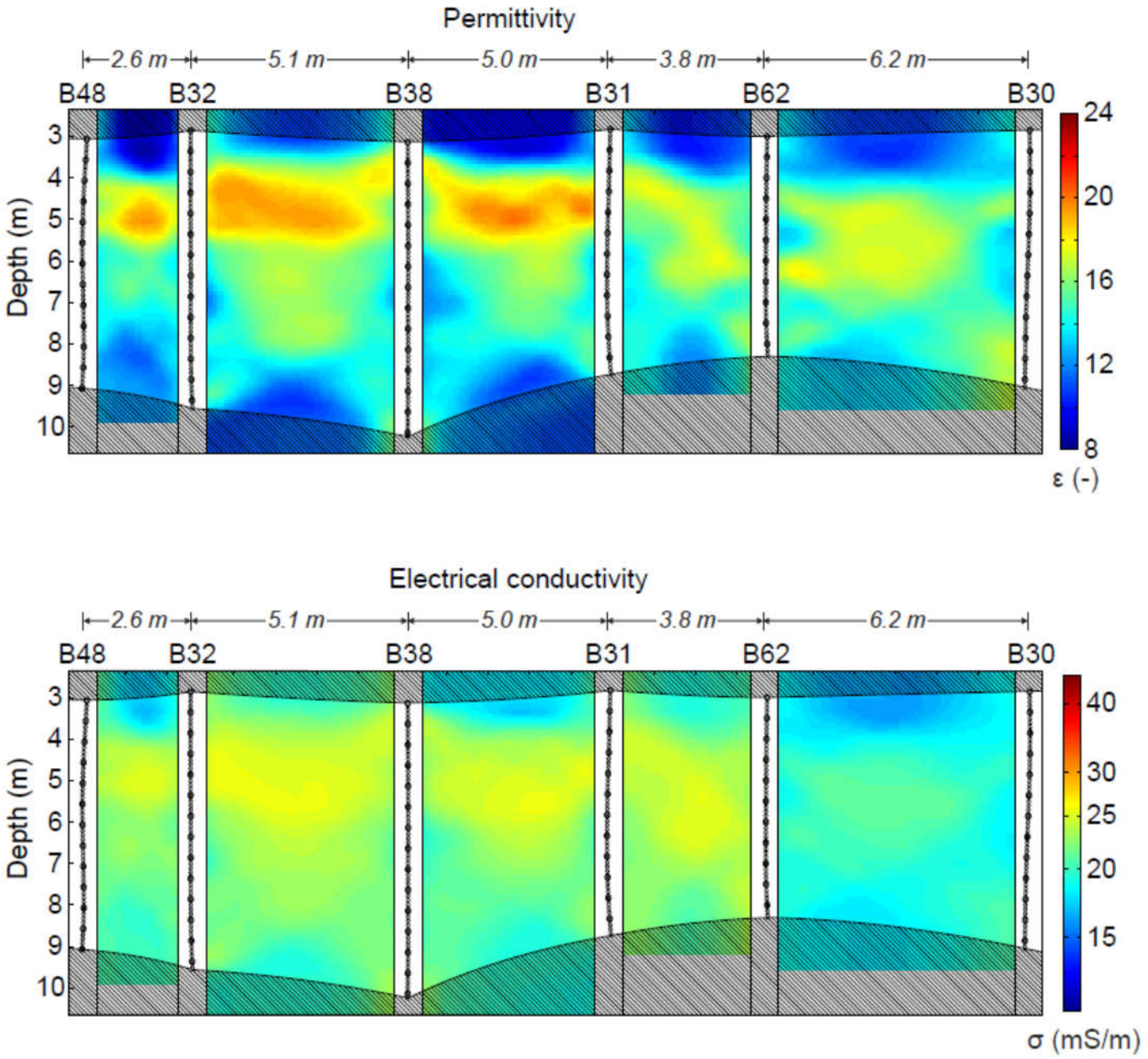

Figure 4. (a) Ray-based relative permittivity and (b) conductivity inversion results of five crosshole planes covering a total range of 25 m length and 10 m depth.

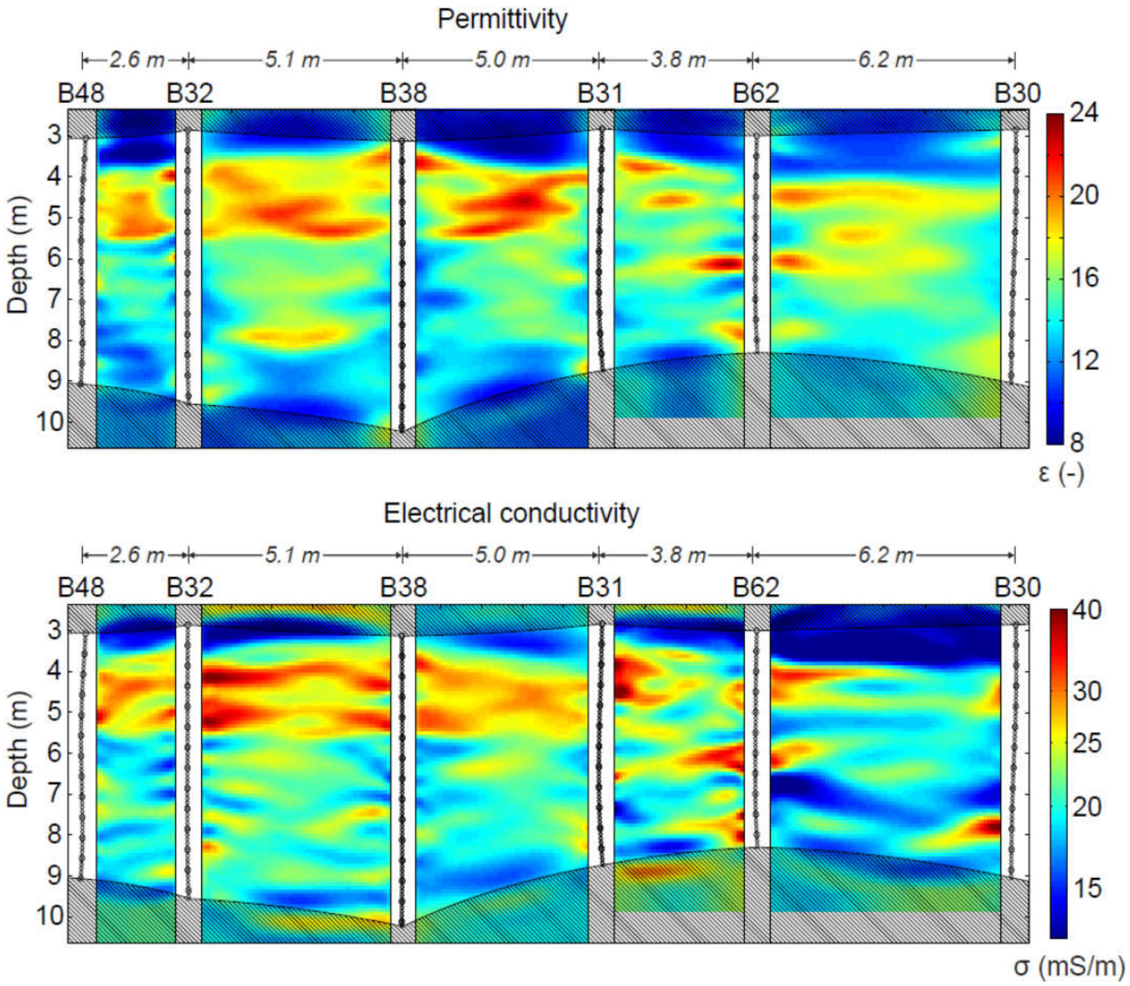

Figure 5. (a) relative permittivity and (b) conductivity results obtained by full-waveform inversion. The white areas between the planes indicate the region where the gradients are muted.

Here, we compare the obtained ray-based relative permittivity and conductivity inversion results shown in Figure 4 with the corresponding full-waveform inversion results shown in Figure 5. The full-waveform inversion results clearly show improved resolution images compared to the ray-based images. Since the gradients have a high sensitivity close to the sources, artefacts can arise close to the boreholes resulting in unreliable inversion results. Therefore, the gradients of 7 cells (7 x 9 cm = 63 cm) around each borehole are muted during the inversion (see Figure 5). However, relatively large amplitude conductivity changes are still present close to the boreholes.

To reduce these artefacts and prevent a relatively large tapering, the gradients $\nabla\bar{S}_\varepsilon$ and $\nabla\bar{S}_\sigma$ are preconditioned with the maximum values of the forward propagated field and the back-propagated residual field. The preconditioner operator P^k for the updating domain $\mathbf{x}$ is defined by (see also Kurzmann et al., 2013)

$$P^k(\boldsymbol{x}) = \frac{b(\boldsymbol{x})}{max_{\boldsymbol{x}}\, b(\boldsymbol{x})} \tag{5}$$

where

$$b(\boldsymbol{x}) = \frac{1}{a(\boldsymbol{x})+C_{stab}\bar{a}} \tag{6}$$

and

$$a(x) = max_t|E^s| + max_t|\hat{G}^T[\Delta E^s]| \tag{7}$$

Here, $\bar{a}$ denotes the spatial average of $a(\boldsymbol{x})$, and $C_{stab}=10$ stabilizes the computation of P^k and was manually estimated (see also Kurzmann et al., 2013).

Applying this gradient enables a reduction of the muted domain to 3 cells (3 x 9 cm= 27 cm), which corresponds approximately to the drilling diameter of about 30 cm. Note that the soil material within this drilling diameter is strongly disturbed due to the drilling, casing, water-filled plastic tubes, etc. The obtained full-waveform inversion results (see Figure 6) contain smaller blank areas around the boreholes and the artefacts close to the boreholes are strongly reduced. More research is needed to optimize the parameterization of this preconditioning and to compare the obtained results with ground truth borehole Neutron-Neutron and electrical conductivity logs.

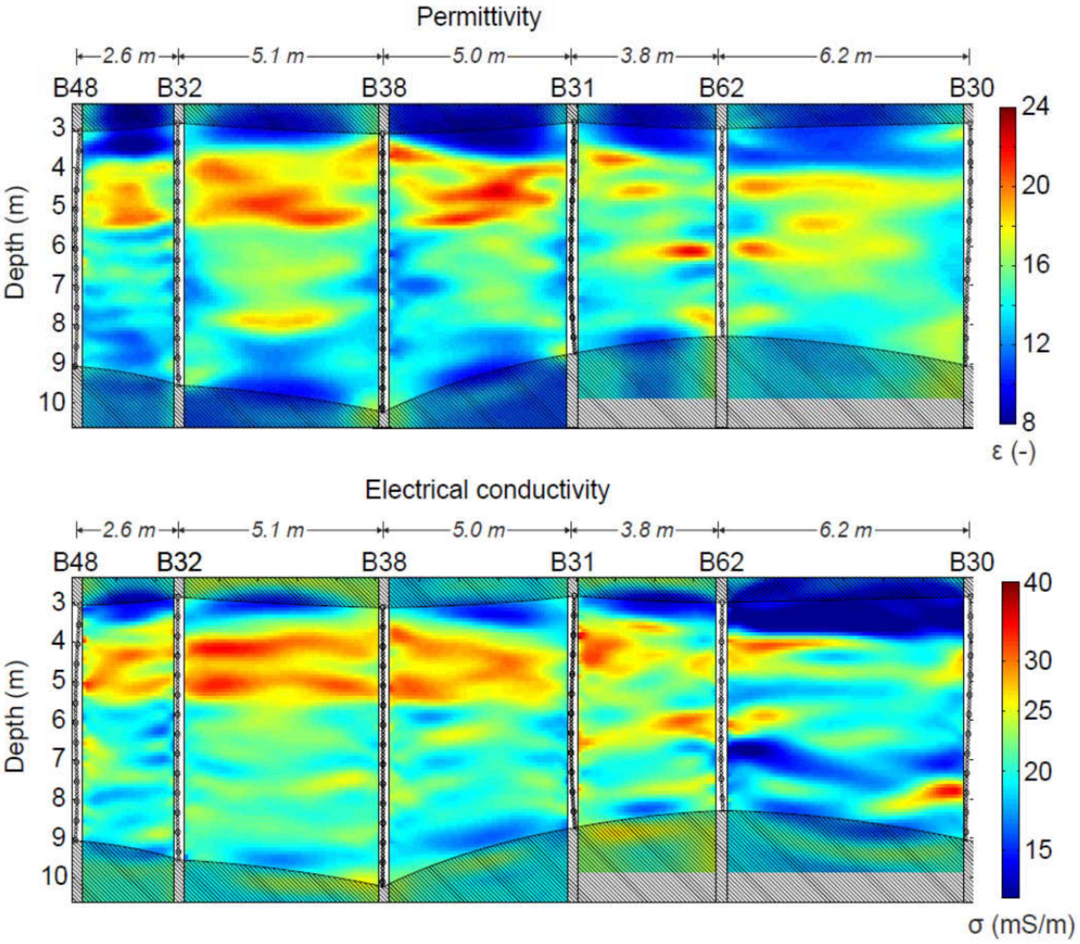

Figure 6. (a) Relative permittivity and (b) conductivity results obtained by full-waveform inversion using a preconditioned gradient. The white areas between the planes are strongly reduced and less artefacts are present close to the boreholes.

Figure 7 (a) shows the measured data for receivers present in borehole 30 and sources present in borehole 62 and allows a comparison with the modelled data obtained using the (b) ray-based inversion, (c) full-waveform inversion without gradient preconditioning, and (d) the full-waveform inversion with gradient preconditioning. The modelled data using the ray-based inversion results show similar first arrival times, however, the small-scale amplitude changes present in the measured data are not reconstructed. This is due to the use of only the first arrival time and first cycle amplitudes to obtain the inversion results shown in Figure 4. In contrast, the modelled data using the full-waveform inversion without and with the preconditioning does explain the measured data well and show similar travel-time and amplitude changes. Note that all the data shown in Figure 7(a) is used to obtain the full-waveform inversion results shown in Figures 5 and 6.

(a) Measured data

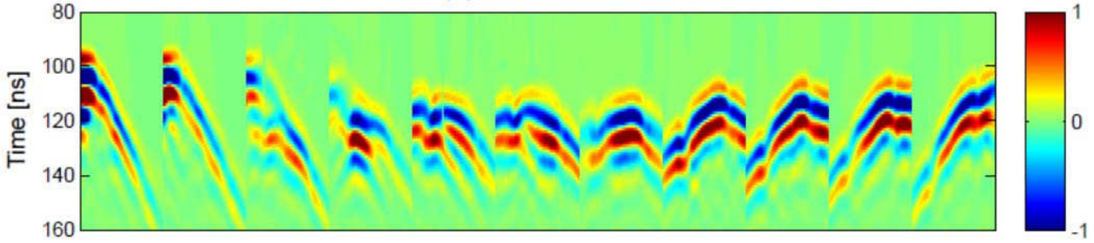

(b) Ray-based modelled data

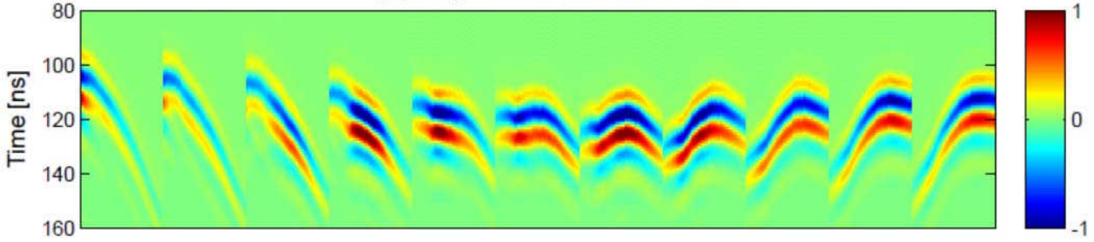

(c) Full-waveform modelled data (with filter)

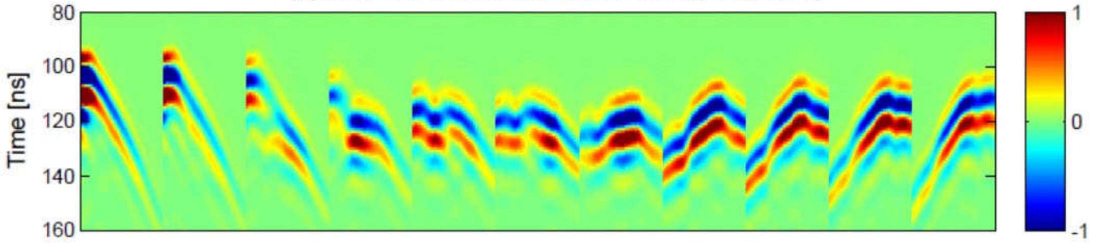

(d) Full-waveform modelled data (without filter)

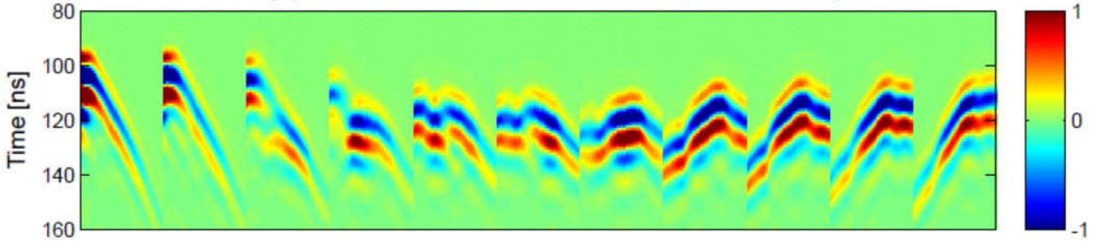

Figure 7 (a) Measured data for receivers present in borehole 30 and sources present in borehole 62, modelled data using the (b) ray-based inversion (c) full-waveform inversion without gradient preconditioning, and (d) full-waveform inversion with gradient preconditioning.

Conclusions & Outlook

High-resolution, sub-wavelength information can be obtained from EMI and GPR data by using inversion tools that are based on exact vectorial electromagnetic wave approaches. A novel three-layer EMI inversion algorithm has been used that employs the different sensing depths of multi-configuration EMI data. After proper calibration, the three-layer medium properties are reconstructed using an efficient parallelized global minimization algorithm and a full-solution horizontally layered EM forward model. Inversion of these calibrated multi-configuration EMI data provides lateral and vertical conductivity variations very similar to those observed in an elaborate ERT experiment. Since for every grid location the data are independently inverted and stitched together to form a quasi-3D image, this inversion could be parallelized to invert large scale EMI data. Full-waveform inversion of crosshole GPR data returns significantly higher resolution images than conventional ray-based images and better depicts the medium properties within the subsurface. The use of a preconditioning of the gradient reduces artefacts close to the source locations and improves the obtained results. A good amplitude and phase fit between the measured and modeled data using the full-waveform inversion results was obtained, indicating the reliability of the full-waveform inversion results. Currently the full-waveform inversion is being extended for on-ground GPR data which can then be combined with the multi-configuration EMI inversion and will extend the possible range of applications significantly. The obtained results show novel inversion algorithms that are based on a high resolution modeling program can exploit the full information content present in the data which enables the unprecedented high resolution characterization of the subsurface.

Acknowledgements

We acknowledge the SFB/TR32 'Patterns in Soil-Vegetation-Atmosphere Systems: Monitoring, Modelling and Data Assimilation', 'TERestrial ENvironmental Observations' (TERENO), and the CROP.SENSE.net research network.

References

Abdu, H., Robinson, D.A., Seyfried, M., and Jones, S.B., 2008, Geophysical imaging of watershed subsurface patterns and prediction of soil texture and water holding capacity: *Water Resources Research* 44, WR007043.

Ernst, J.R., Maurer, H.R., Green, A.G., and Holliger, K., 2007, Full-waveform inversion of cross hole radar data based on 2-D finite-difference time-domain solutions of Maxwell's equations: *IEEE Transactions on Geoscience and Remote Sensing*, 45, 2807-2828.

Gueting, N., Klotzsche, A., van der Kruk, J., Vanderborght, J., Vereecken, H., Englert, A., 2015, Imaging and characterization of facies heterogeneity in an alluvial aquifer using GPR fullwaveform inversion and cone penetration tests, *Journal of Hydrology*, 524, 680–695, doi:10.1016/j.jhydrol.2015.03.030.

von Hebel, C., Rudolph, S., Mester, A., Huisman, J. A., Kumbhar, P., Vereecken, H., van der Kruk, J., 2014, Three-dimensional imaging of subsurface structural patterns using quantitative large-scale multi-configuration electromagnetic induction data, *Water Resources Research*, 50, 2732-2748.

Klotzsche, A., van der Kruk, J., Meles, A.G., Doetsch, J., Maurer, H. and Linde, 2010, N., Full-waveform inversion of crosshole ground penetrating radar data to characterize a gravel aquifer close to the river Thur, Switzerland: *Near Surface Geophysics*, 8, 631-646,.

Klotzsche, A., van der Kruk, J., Meles, A.G., Vereecken, H., 2012, Imaging of preferential flow paths within aquifer systems using crosshole GPR Full-waveform inversion: *Geophysics*, 77 , H57-H62.

Klotzsche, A., van der Kruk, J., Linde, N., Doetsch, J., Vereecken, H., 2013, 3D characterization of high-permeability zones in a gravel aquifer using 2D crosshole GPR full-waveform inversion and waveguide detection: *Geophysical Journal International*, 195, 932-944.

Klotzsche, A., van der Kruk, J., Bradford, J., Vereecken, H., 2014, Detection and identification of high contrast layers with limited lateral extent using an amplitude analysis approach and crosshole GPR full-waveform inversion: synthetic and experimental data, *Water Resources Research*, 50, 6966-6985.

Kurzmann, A., Przebindowska, A., Köhn, D. and Bohlen, T., 2013, Acoustic full waveform tomography in the presence of attenuation: a sensitivity analysis, *Geophysical Journal International*, 195, 985-1000.

Lavoué, F., van der Kruk, J., Rings, J.,André, F., Moghadas, D., Huisman, J.A., Lambot, S., Weihermüller, L., Vanderborght, J., and Vereecken, H., 2010, Electromagnetic induction calibration using electrical conductivity modeling based on electrical resistivity tomography: *Near Surface Geophysics*, 8, 3- 11.

Lavoué, F., R Brossier, L Métivier, S Garambois, J Virieux, 2014, Two-dimensional permittivity and conductivity imaging by full waveform inversion of multioffset GPR data: a frequency-domain quasi-Newton approach, *Geophysical Journal International*, 197, 248-268.

Meles, G.A., van der Kruk, J., Greenhalgh, S.A., Ernst, J., Green, A.G. and Maurer, H., 2010, A new vector waveform inversion algorithm for simultaneous updating of conductivity and permittivity parameters from combination crosshole/Borehole-to-surface GPR data: *IEEE Transactions on Geoscience and Remote Sensing*, 48, 3391-3407.

Meles, G.A., Greenhalgh, S., van der Kruk, J., Green, A.G., and Maurer, H., 2011, Taming the non-linearity problem in GPR full-waveform inversion for high contrast media, Journal of Applied Geophysics, 73, 174-186.

Mester, A., van der Kruk, J., Zimmermann, E., Vereecken, H., 2011, Quantitative two-layer conductivity inversion of multi-configuration electromagnetic induction measurements, *Vadose Zone Journal*, 10, 1319-1330.

Nüsch, A. K., P. Dietrich, U. Werban, and T. Behrens, 2010, Acquisition and reliability of geophysical data in soil science, 19th World Congress of Soil Science, Solutions for a Changing World.

Oberrohrmann, M., Klotzsche, A., Vereecken, H., van der Kruk, J., 2013, Optimization of acquisition setup for cross-hole GPR full-waveform inversion using checkerboard analysis, *Near Surface Geophysics*, 11, 197-209.

Robinson, D.A., I. Lebron, S.M. Lesch, and P. Shouse, 2004, Minimizing drift in electrical conductivity measurements in high temperature environments using the EM-38, *Soil Sciences Society of America Journal* 68, 339–345.

Rudolph, S., J. van der Kruk, C. von Hebel, M. Ali, M. Herbst, C. Montzka, S. Pätzold, D.A. Robinson, H. Vereecken, and L. Weihermüller, L., 2015, Linking satellite derived LAI patterns with subsoil heterogeneity using large-scale ground-based electromagnetic Induction measurements, *Geoderma*, 241-242, 262-271.

Saey, T., De Smedt, P., Islam, M. M., Meerschman, E., De Vijver, E. V., Lehouck, A., and Van Meirvenne, M., 2012, Depth slicing of multi-receiver EMI measurements to enhance the delineation of contrasting subsoil features, *Geoderma*, 189, 514-521.

Santos, F.A.M., Triantafilis, J., Bruzgulis, K.E., and Roe J.A.E., 2010, Inversion of multi–configuration electromagnetic (DUALEM-421) profiling data using a one-dimensional laterally constrained algorithm, *Vadose Zone Journal* 9, 117–125.

Stadler, A., Rudolph, S., Kupisch, M., Langensiepen, M., van der Kruk, J., Ewert, F., Quantifying the effects of soil variability on crop growth using apparent soil electrical conductivity measurements, *European Journal of Agronomy*, 64, 8-20.

Virieux, J. and Operto, S., 2009, An overview of full-waveform inversion in exploration geophysics: *Geophysics*, 74, WCC1–WCC26.

Yang, X., Klotzsche, A., Meles, G., Vereecken, H., and van der Kruk, J., 2013a, Improvements in crosshole GPR full-waveform inversion and application on data measured at the Boise Hydrogeophysics Research Site: *Journal of Applied Geophysics*, 99, 114-124.

Yang, X., Klotzsche, A., van der Kruk, J., Bikowski, J., Kumbhar, P, Meles, G.A., and Vereecken, H., 2013b, Frequency-domain Full-waveform Inversion of GPR Data: *Near-surface geophysics and environment protection*, 344-348.